140 H/D Isotopomers Identified by Long-Range NMR Hyperfine Shifts in Ruthenium(III) Ammine Complexes. Hyperconjugation in Ru-NH3 Bonding

6 AUTHORS, INCLUDING:

William Michael. Laidlaw
University of Oxford
15 PUBLICATIONS **465** CITATIONS

SEE PROFILE

Jennifer C Green
University of Oxford
393 PUBLICATIONS **8,785** CITATIONS

SEE PROFILE

Jeffrey Harmer
University of Queensland
66 PUBLICATIONS **1,460** CITATIONS

SEE PROFILE

140 H/D Isotopomers Identified by Long-Range NMR Hyperfine Shifts in Ruthenium(III) Ammine Complexes. Hyperconjugation in Ru–NH₃ Bonding

W. Michael Laidlaw,*[†] Robert G. Denning,[†,∞] Jennifer C. Green,*[†] Jonathan Boyd,[‡] Jeffrey Harmer,[§] and Amber L. Thompson[⊥]

[†]Department of Chemistry, [‡]Department of Biochemistry, [§]Center for Advanced Electron Spin Resonance, Department of Chemistry, [⊥]Chemical Crystallography, Department of Chemistry, University of Oxford, South Parks Road, Oxford OX1 3QR, United Kingdom

S *Supporting Information*

^{1}H NMR 950 MHz; 50% D$_2$O (aq) $S = 0$ $S = \frac{1}{2}$ R$_3$ = H$_x$D$_{3-x}$ (x = 0 - 3)
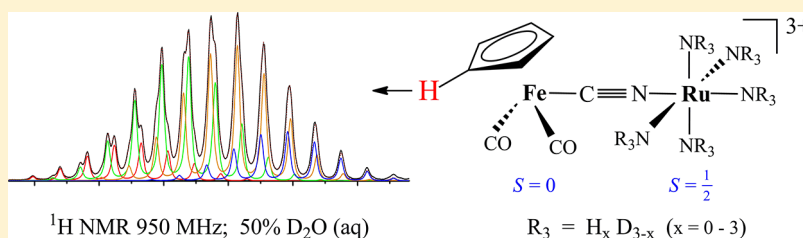
ABSTRACT: ^{1}H NMR spectra of the paramagnetic cyanide-bridged mixed-valence compound $[(\eta^5\text{-}C_5H_5)Fe(CO)_2(\mu\text{-}CN)Ru(NH_3)_5](CF_3SO_3)_3$ (**I**) have been obtained in several solvents. When traces of partially deuterated water are present, instead of a single cyclopentadienyl (Cp) resonance shifted by the hyperfine interaction, numerous well-resolved resonances are observed. The spectra were simulated satisfactorily by giving the appropriate statistical weight to 140 possible H/D isotopomers formed by deuteration in the five ruthenium(III) ammine ligands. The proliferation of distinct resonances occurs because (a) the hyperfine shifts (HSs) due to each sequential deuteration in a single ammine are different and (b) while deuteration in an ammine cis to the cyanide bridge causes a downfield shift, in the trans ammine it causes an upfield shift that is nearly twice as large. All of these shifts exhibit a $1/T$ dependence, but temperature-independent components, due to large second-order Zeeman effects at the Ru^{III} center, are also present. Combining the results of density functional theory calculations with data from metal–metal charge-transfer optical transitions and with the effect of solvent-induced NMR HSs, it is argued that Fermi contact shifts at the Cp protons are insignificant compared to those due to the dipolar (pseudocontact) mechanism. Analytical expressions are presented for the dependence of the HS on the tetragonal component of the ligand field at the Ru^{III} ion. The tetragonal field parameter, defined as the energy by which the 4d$_{xy}$ orbital exceeds the mean t$_{2g}$ orbital energy, was found to be 147, 52, and 76 cm^{-1}, in dimethylformamide, acetone, and nitromethane, respectively. The effects of deuteration show that there is a significant component of hyperconjugation in the Ru–ammine interaction and that ND$_3$ is a weaker π donor than NH$_3$. A single deuteration in an axial ammine increases the tetragonal field parameter (ν) by +2.8 cm^{-1}, resulting in a HS of −37 ppb in the Cp proton resonance, whereas a single deuteration in an equatorial ammine decreases the field by −1.5 cm^{-1} with a HS of +20 ppb, despite a nominal separation of seven chemical bonds. We analyze the origin of this remarkable sensitivity, which relies on the favorable characteristics of the Ru^{III} low-spin t$_{2g}^5$ configuration, having a spin–orbit coupling constant $\zeta \approx 950$ cm^{-1}.

1. INTRODUCTION

In recent publications, we have explored the extent of charge and spin transfer across cyanide-bridged bimetallic complexes by various means, including the nuclear hyperfine interaction.[1,2] These compounds contain a nominally 18-electron diamagnetic metal donor and a low-spin paramagnetic Ru^{III} or Os^{III} d^5 acceptor. They belong in class II of the Robin–Day classification; i.e., the extent of charge and spin transfer is small.[3] In the course of this work, we were surprised to find an extensive group of multiple resonances in the NMR spectrum for a set of magnetically equivalent protons on a cyclopentadienyl (Cp) ring bound to the diamagnetic metal that could be attributed to partial deuteration in the five ammine

ligands coordinated to a paramagnetic Ru^{III} ion: a proton–proton separation of seven bonds.

Examples in which large so-called "secondary" isotope shifts have been observed in the NMR spectra of partially deuterated paramagnetic compounds are rare. Well-separated ^{13}C resonances are observed for each of the five isotopomers obtained by deuterium substitution of the bridging hydrides in the cubane-like paramagnetic cluster $\{Cp''Cr(\mu_3\text{-}H)\}_4$ (Cp'' = η_5-C$_5$Me$_4$Et).[4] In the ^{1}H NMR spectra of iron(III) protoporphyrins substituted by peripheral methyl and vinyl groups, partial deuteration in the vinyl β position introduces shifts of ~30 ppb

in the proton resonances of a methyl group in the same pyrrole ring, as well as in those in rings adjacent or opposite to that where the substitution is made. The signs of these shifts are compatible with a perturbation of the orthorhombic component of the ligand field at the iron atom.[5] Monodeuteration of a pyrrole ring in iron(III) tetraphenylporphyrins has similar consequences, and a comparison with other substituents implies that the deuterium atom is a slightly stronger σ donor than the hydrogen atom.[6] In each of these cases, it is not easy to identify the electronic features that underlie the perturbation in the hyperfine interaction. Here we present ^{1}H NMR data for the bimetallic cyanide-bridged complex $[(\eta^5\text{-}C_5H_5)Fe(CO)_2(\mu\text{-}CN)Ru(NH_3)_5]^{3+}$ (**I**), which displays sufficient spectroscopic detail to permit a fuller analysis of the electronic origin of these isotope shifts.

2. METHODS

2.1. Synthesis of $[(\eta^5\text{-}C_5H_5)Fe(CO)_2(\mu\text{-}CN)Ru(NH_3)_5]$-$(CF_3SO_3)_3$ (I). $(\eta^5\text{-}C_5H_5)Fe(CO)_2Br$ was prepared from $[(\eta^5\text{-}C_5H_5)Fe(CO)_2]_2$ as described elsewhere[7,8] and purified as a toluene solution adsorbed on a neutral activated alumina (Brockmann I) chromatography column followed by elution with dichloromethane or chloroform. It was recrystallized from a chloroform solution by adding hexane. $(\eta^5\text{-}C_5H_5)Fe(CO)_2CN$ [and $(\eta^5\text{-}C_5H_5)Fe(CO)_2{}^{13}CN$] was prepared from the bromide according to the literature[7] and purified in the same way as the bromide. Compound **I** (with and without ^{13}C cyanide enrichment) was synthesized by dissolving a slight excess of $(\eta^5\text{-}C_5H_5)Fe(CO)_2CN$ (0.1 g, 0.493 mmol) with $Ru(NH_3)_5(OSO_2CF_3)(CF_3SO_3)_2$ (0.27 g, 0.426 mmol), prepared as described previously,[8] in ~25 mL of high-performance liquid chromatographic acetone under nitrogen. After stirring in the dark for 2−3 days, the red-orange solution was evaporated to dryness at room temperature in the dark. The residue was dissolved in 1−2 mL of acetone and the product precipitated by adding excess dichloromethane and then diethyl ether. The orange solid was filtered, washed with diethyl ether, and dried under vacuum. Yield: ~0.34 g. The complex was recrystallized by dissolving in a minimum volume of acetone, adding absolute ethanol (~2 mL), and cooling to −20 °C. $[(\eta^5\text{-}C_5H_5)Fe(CO)_2(\mu\text{-}CN)Ru(NH_3)_5](CF_3SO_3)_3$. Anal. Found (calcd): C, 15.8 (15.9); H, 2.5 (2.4); N, 9.9 (10.0). IR (KCl): 2152 (^{12}CN), 2111 (^{13}CN), 2071, 2029 (CO) cm^{-1}. ^{13}C NMR (20 mg in 580 μL of acetone-d^6 with 15 μL of 90:10 H/D water): δ 94.36 (C_5, multiple resonances), 122.87 (CF_3, $^1J(C-F) \sim 318$ Hz), 256.72 (CO), 898.6 (CN fwhm ~1700 Hz). $(\eta^5\text{-}C_5H_5)Fe(CO)_2CN$. IR (KCl): 2118 (^{12}CN), 2075 (^{13}CN), 2062, 2005 (br) (CO) cm^{-1}. Compound **I** slowly darkens in sunlight in the solid state but is more photosensitive in solution; it should be manipulated and stored in the dark. The rhodium analogue $[(\eta^5\text{-}C_5H_5)Fe(CO)_2(\mu\text{-}CN)Rh(NH_3)_5](CF_3SO_3)_3$ (with ~25% ^{13}CN enrichment) was prepared analogously using $[Rh(NH_3)_5(OSO_2CF_3)](CF_3SO_3)_2$ as the precursor[9] to give a pale-yellow solid. Anal. Found (calcd): C, 15.7 (15.8); H, 2.5 (2.4); N, 9.9 (10.0). IR (KBr): 2179 (^{12}CN), 2134 (^{13}CN), 2063, 2025 (CO) cm^{-1}. ^{13}C NMR (acetone-d^6): δ 88.07 (C_5), 121.74 (CF_3, $^1J(C-F) \sim 318$ Hz), 148.08 (CN, $^2J(C-Rh) \sim 3.9$ Hz), 210.40 (CO, $^2J(C-{}^{13}CN) \sim 11.6$ Hz).

2.2. X-ray Crystallography. Crystals of **I** suitable for X-ray crystallography were grown by cooling a nitromethane solution to −20 °C. Single-crystal diffraction data were collected using a Nonius Kappa CCD diffractometer with a graphite-mono-chromated Mo Kα source (λ = 0.71073 Å). A representative single crystal was selected and mounted on a hair using perfluoropolyether oil. The crystal was then rapidly cooled to 150 K using an Oxford CryoSystems CryoStream 600.[10] Raw frame data were reduced using *DENZO-SMN/SCALEPACK*,[11] including unit cell parameter refinement, interframe scaling, corrections for the Lorentz effect, and absorption. The crystal structure was solved using *SIR92*[12] within the *CRYSTALS* structure refinement suite[13] to give the atomic positions for the cation and anions. Examination of the difference Fourier map and initial refinement indicated the presence of water of crystallization. Further refinement yielded a residual electron density and prolate displacement ellipsoids that severely failed the Hirshfeld condition affecting one of the triflate anions, suggesting the presence of disorder. This was modeled with the triflate occupying a position split over two sites with 36(2)% occupancy for the minor component; however, restraints were required to maintain a sensible geometry and displacement ellipsoids. Despite the disorder, the hydrogen atoms were visible in the difference Fourier map and refined with restraints prior to inclusion in the final refinement with a riding model.[14] Distances and angles to the planes were calculated with *PLATON*.[15,16] The final structure was refined using full-matrix least squares to give R1 = 0.0434, wR2 = 0.0939 (from all 7029 reflections), ρ_{min} = −0.94 e·Å^{-3}, and ρ_{max} = 0.66 e·Å^{-3}.

Full structural data are included in the Supporting Information (SI) and have been submitted to the CCDC (CCDC 932615). These data can also be obtained free of charge from The Cambridge Crystallographic Data Centre via http://www.ccdc.cam.ac.uk/data_request/cif.

2.3. NMR Spectroscopy. The ^{1}H NMR experiments in aqueous conditions were performed on a 950 MHz spectrometer operating at 298 K equipped with a probe head incorporating three axis gradients and optimized for ^{1}H detection. The measurements used 1,4-dioxane as an internal reference with a proton chemical shift of 3.75 ppm. To observe the long-range $^7\Delta^1H(^{2/1}H)$ deuterium-induced isotope shifts in the equivalent protons of the Cp ring, which resonate quite close to the intense signal of the water protons, suppression techniques were applied using the pulse-field-gradient double-echo method described by Hwang and Shaka[17] with the ^{1}H carrier on the H$_2$O resonance. The refocusing element included a 3 ms Gaussian-shaped 180° pulse applied at the solvent resonance frequency. The time domain data were recorded with 16384 complex points, an interscan delay of 2.5 s, 32 scans per free induction decay, and an acquisition time of 1.31 s and were zero-filled prior to Fourier transformation.

Observation of the broad ^{1}H signals from the axial (~+172 ppm) and equatorial (~+143 pm) paramagnetic shifted ammine isotopomer resonances required presaturation of the solvent signal, with a weak on-resonance radio-frequency field for 0.7 s, prior to positioning the ^{1}H carrier +157.1 ppm downfield of the solvent resonance for detection. These time domain data were recorded with 4096 complex points, an interscan delay of 0.725 s, and an acquisition time of 69.6 ms and were strongly resolution-enhanced with a Lorentzian−Gaussian function and zero-filled prior to Fourier transformation.

^{1}H NMR experiments in nonaqueous solvents, and at variable temperatures, were done on a Varian 500 MHz instrument with resonances referenced to tetramethylsilane (TMS) at ~300 K. Temperatures were calibrated using a methanol reference sample. ^{13}C NMR (125.7 MHz) experi-

ments at 298 K (in acetone-d^6, reference 29.9 ppm) were undertaken on a Bruker AVII 500 spectrometer fitted with an optimized cryoprobe.

2.4. Electron Paramagnetic Resonance (EPR) Spectroscopy. W-band (93.9031 GHz) echo-detected EPR experiments were performed at 7.5 K on a Bruker BioSpin GmbH EMX spectrometer equipped with a Bruker EN600-1021H TeraFlex W-band pulsed ENDOR resonator and an Oxford Instruments helium-flow cryostat. The echo-detected field sweep was recorded with the pulse sequence $\pi/2-\tau-\pi-\tau-$ echo ($t_{\pi/2}$ = 32 ns, t_{π} = 64 ns, and τ = 160 ns) by monitoring the integrated echo intensity versus field. The field was calibrated with an ENDOR measurement using the known position of the ^{1}H Larmor frequency. The EPR spectrum was simulated with *Easyspin* using a rhombic **g** matrix with principal values **g** = [2.2537, 2.0315, 1.7565] and Gaussian line widths L = 7010, 11450, and 21500 MHz, where fwhm = $L/(2 \ln 2)^{1/2}$.

2.5. Computational Methods. The geometry of the gas-phase cation **I** was optimized using the B3LYP functional[11−14] and a SDD basis set[18] employing the Gaussian code.[19] Further calculations used the Amsterdam Density Functional program suite *ADF 2010.2*.[20−22] Relativistic corrections were included via the zeroth-order relativistic approximation (ZORA) method for all calculations.[23−26] The sensitivity of the spin density to various functionals was tested using a TZ2P basis set. The *g* values were calculated using a spin−orbit calculation and the electron spin resonance program.[27,28] The effect of solvation by different solvents was modeled by the conductor-like screening model (COSMO) method[29−32] by using the BP functional and TZ2P basis sets with frozen small cores. Explicit solvation was modeled both by including five explicit water molecules hydrogen-bonded to the five ammines and also by using the COSMO model with parameters for water as the solvent. The positions of the water molecules were optimized while retaining the gas-phase geometry of the cation. For the explicit solvation model, the B3LYP functional was again employed together with all-electron TZP basis sets. Cartesian coordinates for optimized structures are given in the SI, together with a comparison of the calculated and experimental structural data and spin densities for the metal atoms.

3. RESULTS

3.1. Molecular Geometry. The main structural features of the cation in compound **I** are shown in Figure 1 and Table 1. The cyanide bridge is close to linear, and with the exception of the Cp ring, the other ligands subtend angles close to 90° at the metal atoms with respect to both the bridge and one another. The centroid of the ring subtends an angle at the iron atom close to 120° with respect to the bridge. The difference between the axial and equatorial Ru−N bond lengths is small. The carbonyl groups adopt a staggered conformation with respect to the ammines containing N3, N4, and N5, while C4, H4, Fe, C1, N1, N2, N4, and N6 together define a plane (*XZ*) with close to mirror symmetry. Notice that the orientation of the Cp ring minimizes nonbonded interactions between ring protons H6 and H7 and the N2 ammine group.

3.2. NMR Spectroscopy: the Cp Proton Resonance. In deuteroacetone solutions of **I**, the Cp proton resonance near 6 ppm resembles a 16-line multiplet. However, if the acetone-d_6 is dried in situ (i.e., in the NMR tube) over an activated molecular sieve, only a single resonance appears in this region. The multiple resonances reappear when traces of H_2O/D_2O mixtures are added; they are the result of distinct hyperfine
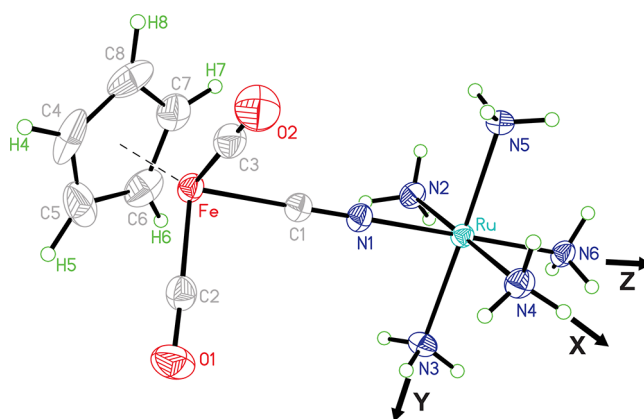

Figure 1. Crystal structure of compound **I**, with displacement ellipsoids drawn at the 50% probability level and the anions and water of crystallization omitted for clarity.

shifts (HSs) in the various H/D isotopomers formed by partial deuteration of the five ammine ligands. Traces of D_2O in commercial deuteroacetone, presumably the result of a keto−enol equilibrium involving residual water, enable this exchange, which is consistent with the rapid (<1 s) proton exchange of ruthenium(III) hexaammine complexes in neutral aqueous solutions.[33,34] At high fields (950 MHz), more than 20 separate proton resonances can be identified; while some isotopomers exhibit upfield shifts in the Cp resonances relative to the fully protonated (H15) species, in others there is a downfield shift. We have found similar structures in the spectra of several related compounds containing the −C≡NM(NH$_3$)$_5^{3+}$ (M = Ru, Os) group. In the [CH$_3$C≡NRu(NH$_3$)$_5$]$^{3+}$ cation, for example, the predominant interval (at 500 MHz) of ∼135 ppb between the methyl resonances associated with a single deuterium substitution in an ammine ligand is substantial.

For compound **I**, multiple resonances can be observed in a variety of deuterated solvents as well as acetone, e.g., nitromethane, acetonitrile, dimethylformamide (DMF), and dimethyl sulfoxide, provided that a trace of the D_2O/H_2O mixture is added to enable partial exchange with the ammine protons.

To examine these isotope-induced shifts under higher resolution, the ^{1}H NMR spectra of **I** at 950 MHz in H_2O/D_2O mixtures were measured at 298 K, using instrumental conditions that completely suppress the HOD and H_2O resonances.[17] The ammine−proton exchange rate is base-catalyzed,[33] and in neutral solutions, the isotopomer structure near 6 ppm collapses to a single line due to rapid H/D exchange. Measurements were therefore made at pH 2, where there is no evidence of exchange broadening. To establish isotopic equilibrium, samples were made up in 0.55 mL of neutral H_2O/D_2O mixtures and then acidified to pH ∼2 by adding 10 μL of a 0.55 M solution of CF$_3$SO$_3$H in the same solvent mixture. Measurements were made on solutions with nominal compositions of 0, 5, 10, 35, 50, 65, 90, 95, and 100% D_2O.

Figure 2 illustrates the spectra in solutions containing 5, 35, 50, and 95% D_2O and also includes simulations, discussed in detail below, that closely reproduce the experimental spectra.

3.3. Deuterium Isotope Shifts. In ∼5% D_2O, the peak at 5.982 ppm in Figure 2a, labeled (0,0) in red, is that of the fully protonated compound. Monodeuteration in the ammine trans to the bridging cyanide shifts the resonance upfield by ∼37 ppb

Table 1. Selected Bond Lengths (Å) and Angles (deg)

Ru−N(av. 2−5)	2.108(2)	Ru−N6	2.100(2)	Ru−N1	2.019(2)
Fe−C1	1.889(3)	Fe−C2	1.794(3)	Fe−C3	1.791(4)
Fe−C$_5$(centroid)	1.712(2)	N1−C1	1.142(4)	C2−O1	1.129(4)
C3−O2	1.135(4)	Fe−C1−N1	177.5(3)	Ru−N1−C1	179.6(3)
C$_5$(centroid)−Fe−Ru	119.1(2)	C1−Fe−C2	92.55(14)	C1−Fe−C3	93.31(15)
C2−Fe−C3	93.31(15)				

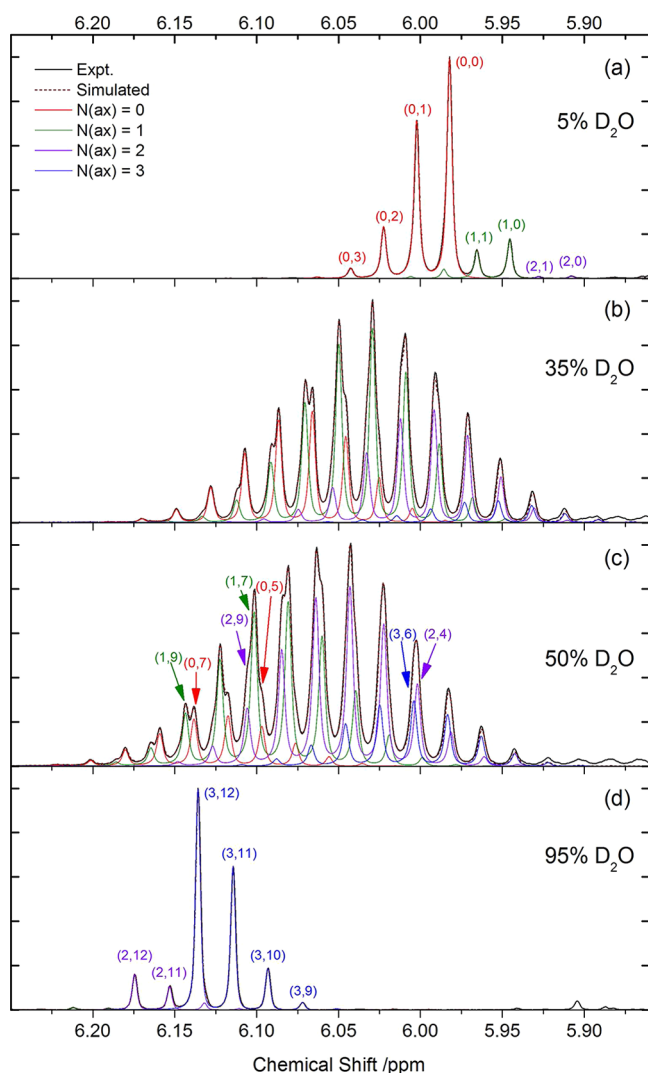**Figure 2.** Experimental (black) and simulated (brown dashed) Cp ^{1}H NMR spectra (950 MHz) of **I** in H$_2$O/D$_2$O mixtures, showing contributions from resonances having 0−3 axial deuterons, colored red, green, purple, and blue, respectively. See the main text for notation. Internal reference (3.75 ppm 1,4-dioxane).

to 5.945 ppm to give the line labeled (1,0) in green, but a single deuteration in a cis ammine (N2−N5 in Figure 1) causes a downfield shift of ∼20 ppb to 6.002 ppm to give the line labeled (0,1) in red. The relative intensity of these resonances is 4:1, as expected on statistical grounds. In the approximate C_{4v} local symmetry of the Ru^{III} cation, the cis and trans ammines are henceforward referred to as *equatorial* and *axial* with respect to the tetragonal (z) axis. Subsequent deuterations are more probable in the equatorial ligands, leading to a progression of lines separated by ∼20 ppb on the downfield side of both (1,0) and (0,1). They are labeled by the number of deuterations in the format (N_{ax}, N_{eq}). The spectrum in 95% D$_2$O (Figure 2d) is

almost a mirror image of that in 5% D$_2$O with the resonance at 6.137 ppm, labeled (3,12) in blue, being that of the fully deuterated compound. A single proton substitution in the deuterated axial ammine of (3,12) now leads to a downfield shift of the line labeled (2,12) in purple to 6.175 ppm, while a single equatorial proton substitution causes an upfield shift of the line labeled (3,11) in blue to 6.115 ppm. The shift for each additional substitution is *roughly* additive so, for any D/H ratio, the spectrum was initially modeled as the sum of the resonances of the 52 distinct species that contain $0 \leq N_{ax} \leq 3$ axial deuterons and $0 \leq N_{eq} \leq 12$ equatorial deuterons.

3.4. Vicinal Effects. In practice, this model proved inadequate and refinements were required to construct the simulations in Figure 2. The simulated resonances for species with N_{ax} = 0, 1, 2, and 3 are colored red, olive-green, purple, and blue, respectively, so the 5% deuterium spectrum is dominated by red and green progressions and the 95% spectrum by purple and blue progressions. Whereas resonances in Figure 2a with N_{ax} = 1 (green) occur 36.71 ppb upfield from those with N_{ax} = 0 (red), those with N_{ax} = 2 (purple) are shifted a further 37.60 ppb upfield. In Figure 2d, the interval between features with equivalent numbers of equatorial deuterons but with N_{ax} = 2 (purple) or 3 (blue) is larger still at 39.59 ppb. Clearly, the effect of vicinal deuterations within a single ammine ligand is not quite additive; the shift due to the second deuteration is greater that the first and that due to the third is greater still.

It follows that the resonance of an isotopomer containing two deuterons in the same equatorial ammine is distinct from one containing two deuterons in different equatorial ammines. If, for example, N_{eq} = 6, there are five different possible configurations. When the nondegeneracy of these configurations is taken into account, there are 35 distinct equatorial ammine isotopomers, each with a distinct resonance. Taking into account that each axial ammine can have 0, 1, 2, or 3 deuterons, this gives 140 possible resonances in all. At any one H/D ratio, many of these are not spectrally resolved, but their contribution to variations in the line width and shape is easily detected.

The probability that any one of these 140 configurations will be present, at a given H/D ratio, is readily calculated. The full spectrum can then be simulated using six variables; ρ_D the percentage of deuterium present in the ammine ligands, δ_0 the chemical shift in the fully protonated compound, $\Delta\delta_{ax}$ the incremental shift due to the introduction of one deuteron into the axial ammonia, $\Delta\delta_{eq}$ its counterpart in an equatorial ammonia, S_2 the fractional increase in either of these shifts when a second deuteron is introduced, and S_3 the factor by which S_2 must be multiplied to obtain the shift upon introduction of a third deuteron in the same ammine. Thus, a configuration containing just three deuterons, all in a single equatorial ammine, would have a resonance at $\delta = \delta_0 + 3\Delta\delta_{eq}(1 + S_2S_3)$, while one containing two axial and one equatorial deuterons would be found at $\delta = \delta_0 + 2\Delta\delta_{ax}(1 + S_2) + \Delta\delta_{eq}$.

Table 2. Fitting Parameters for the Cp Resonances of I in an Aqueous Solution at Nine H/D Ratios

nominal ρ_D	fitted ρ_D	δ_0/ppm	$\Delta\delta_{eq}$/ppb	$\Delta\delta_{ax}$/ppb	S_2	S_3
100	99.650	6.00228	20.1488	−36.7010	0.0230	3.455
95	94.830	6.00005	20.1025	−36.4400	0.0232	3.734
90	90.340	5.99467	20.1504	−36.6950	0.0230	3.567
65	67.192	5.98809	20.1013	−36.4720	0.0250	3.562
50	52.300	5.99509	20.1583	−36.7590	0.0248	3.460
35	36.780	5.98486	20.1574	−36.7330	0.0252	3.574
10	10.670	5.98023	20.0920	−36.6850	0.0260	3.570
5	5.622	5.98222	20.0712	−36.7100	0.0258	3.560
0	0.030	5.97588	20.1740	−36.7600	0.0258	3.560
mean			20.1284	−36.6617	0.0246	3.5602
std dev, %			0.18	0.33	5.03	2.26

Despite the apparent symmetry between parts a and d of Figure 2, significant additional subcomponents are clearly resolved on the low-field features in Figure 2b,c that have no counterparts on the high-field side of the envelope (e.g., ~6.07 ppm in Figure 2b and ~6.135 ppm in Figure 2c). Typically the low-field features have small N_{ax} values and large N_{eq} values, while the reverse is true of the high-field components. Because $\Delta\delta_{eq} \approx +20.1$ ppb and $\Delta\delta_{ax} \approx -36.7$ ppb, it follows that the (1,9) and (0,7) resonances in Figure 2c near 6.135 ppm differ by $\sim 2\Delta\delta_{eq}(1 + S_2) + \Delta\delta_{ax} = 4.4$ ppb, while the (3,6) and (2,4) resonances near 6.010 ppm differ by $\sim 2\Delta\delta_{eq} + \Delta\delta_{ax}(1 + S_2 S_3) = 0.28$ ppb, where we have assumed, *for the purposes of illustration only*, that the most probable number of deuterons per equatorial ligand when $N_{eq} = 7$ or 9 is 2, but it is 1 when $N_{eq} = 4$ or 6. The asymmetry in the resolution of subcomponents on either side of the envelope is thus a direct indication of the nonlinearity stemming from vicinal substitutions on a single ammonia, as expressed in the factors S_2 and S_3. The simulations in Figure 2 compute the positions of the resonances of all of the 35 possible equatorial H/D configurations and use their proper statistical weight.

3.5. Simulation Parameters. In practice, the experimental line shapes show some asymmetry and variability between samples that are attributable, in part, to instrumental inhomogeneity and, in part, to the application of various apodization options. This asymmetry is most obvious in the 0% and 100% D_2O solutions, where a single line dominates the spectrum, so a split Pearson (VII) function[35] was adopted that conveniently describes asymmetrical lines having both Gaussian and Lorentzian contributions. Simulations have been included in Figure 2 for four of the nine samples; their agreement with the experimental spectra is such that, for the most part, they cannot be distinguished within the graphical line widths needed to provide legibility. More generally, the quality of the spectra is sufficient to resolve the resonances of the singly deuterated species (1,0) and (0,1) in a "pure" H_2O solution, in which the natural abundance of deuterium is 0.15% (SI, Figure S1b).

In parts b and c of Figure 2, the simulation upfield of 5.97 ppm is poor because the spectrum is contaminated by the presence of a small amount of impurity (3.7% based on the intensity of the Cp resonances). Its weak spectral features are apparent in all four examples. When H/D ≈ 1, the progressions due to the numerous isotopomers in the impurity overlap those of I in the high-field segments of Figure 2c,d. From its deuteration pattern, the impurity is a compound in which one of the equatorial ammines has been replaced by coordinated water (see an assignment of its spectrum in the SI, Figure S1a). Because it has structure and charge similar to that of I, it is

difficult to remove completely by recrystallization. The sample characterized by chemical analysis in section 2.1, however, was prepared from a separate batch of pentaammineruthenium(III) and does not contain this impurity.

If the region with ≤5.97 ppm in Figure 2c that is contaminated by the impurity is excluded, the simulation gives residual factors $R_a = \sum_i |I_{obs} - I_{calc}|/\sum_i I_{obs} = 2.65\%$ and $R_s = (\sum_i (I_{obs} - I_{calc})^2/\sum_i I_{obs}^2)^{1/2} = 2.76\%$. Similarly, small values are found for the spectra in all nine solvent compositions. The parameters derived from this analysis are summarized in Table 2.

The spectra are accurately reproduced by parameters that vary little across the nine different solutions. The main variations are found in the resonance of the 15-H species (δ_0), which shifts downfield by about 25 ppb in a D_2O solution relative to the same resonance in water and which we take to be due to a progressive decrease in the basicity of the solvent. This assertion is based on the linear dependence of the HS of this resonance on the Gutmann donor number in a variety of solvents. The changing donicity in the *outer sphere* of D_2O versus H_2O will alter the redox potential of the center slightly (vide infra).

3.6. Temperature Dependence. Figure 3 shows the 500 MHz spectra of acetone-d_6 solutions of I at temperatures of −45, −10.5, +16.5, and +42.5 °C. In all, nine measurements were made between −57 and +42.5 °C, giving spectra that could be accurately simulated using the same parametrization scheme as that in Figure 2. Numerical results and actual (calibrated) temperatures are shown in Table 3. The deuterium content in all cases was in the range 16.3 ± 0.2%, except for the spectrum at 299.8 K, where a figure of 17.1% gave a better fit. The values of $\Delta\delta_{eq}$ and $\Delta\delta_{ax}$ in acetone-d_6 at 299.8 K are almost identical with those found in water (Table 1) at 298 K.

To establish a reference from which to derive the HSs in Table 3, as well as those in other solvents, a diamagnetic analogue of I was prepared in which rhodium(III) replaces ruthenium(III) (section 2.1). In this compound, a sharp Cp proton resonance is found (relative to TMS) at 5.332 ppm in D_2O, at 5.409 ppm in acetonitrile-d_3, at 5.435 ppm in nitromethane-d_3, at 5.596 ppm in acetone-d_6, at 5.601 ppm in dimethyl-d_6 sulfoxide, and at 5.659 ppm in DMF-d_7.

3.7. Temperature-Dependent and -Independent Shifts and EPR Measurements. Many years ago, Kurland and McGarvey[36] developed expressions for the HS in transition-metal complexes. Here we rely on that part of their work (SI, section S6) relevant to the present spin $^1/_2$ system in which only a single Kramers doublet ground state (labeled *i*,
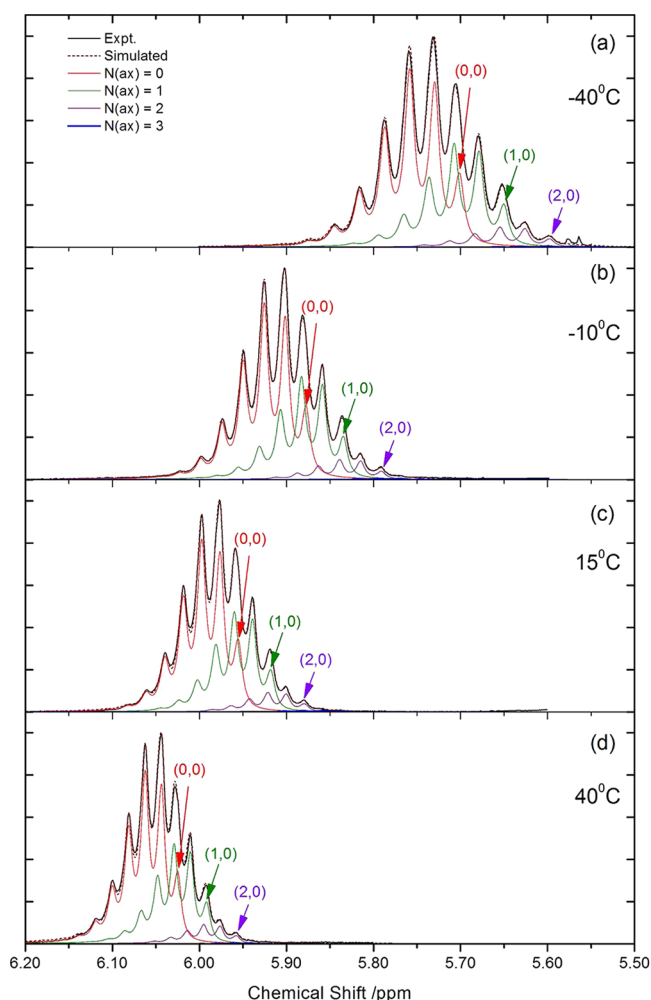
Figure 3. Cp ^{1}H NMR spectrum (500 MHz) of **I** in an acetone-d_6 solution, at nominally (a) −40, (b) −10, (c) +15, and (d) +40 °C. Actual temperatures are given in Table 3. The deuterium content is 16.3%. The plot colors are as in Figure 2.

Table 3. Temperature Dependence of the Fitting Parameters in an Acetone Solution

temp/K	$\Delta\delta_{eq}$/ppb	$\Delta\delta_{ax}$/ppb	δ_0/ppm	HS, δ_p/ppm
315.5	18.720	−33.22	6.02473	0.42873
299.8	19.735	−36.20	5.97687	0.38087
289.5	20.910	−37.39	5.95527	0.35927
274.3	22.510	−40.95	5.91354	0.31754
262.5	24.000	−42.81	5.87730	0.28130
252.0	24.955	−45.47	5.83477	0.23877
240.5	26.511	−47.91	5.78103	0.18503
228.0	28.488	−50.95	5.70094	0.10494
216.0	29.880	−54.96	5.61894	0.02294

with components α and β) is thermally occupied. The orientational average of the HS in solution is given by

$$\delta_h = \frac{1}{3}\sum_{k=x,y,z}\frac{1}{2}\sum_{i=\alpha,\beta}\left\{2\sum_{j'}\frac{\langle i|\hat{\mu}_k|j\rangle\langle j|\hat{A}_k|i\rangle}{\Delta\varepsilon_{ij}}\right.$$
$$\left. -\frac{\langle i|\hat{\mu}_k|i\rangle\langle i|\hat{A}_k|i\rangle}{kT}\right\} \tag{1}$$

where j' indicates all states other than the components of the ground state, $\Delta\varepsilon_{ij} = \varepsilon_i - \varepsilon_j$ is by definition negative, and $\hat{\mu}_k$ and $\hat{A}_k$ are Cartesian vectors representing the magnetic moment and hyperfine field operators, respectively. In eq 1, the temperature-dependent and -independent terms are associated with the first- and second-order electronic Zeeman interactions, respectively, so that at ambient temperatures in an obvious notation

$$\delta_h = \delta^{(1)}(T) + \delta^{(2)} = (b/T) + \delta^{(2)} \tag{2}$$

In solution, the first-order term can be written as the orientational average of the product of the principal values of the hyperfine coupling tensor $\mathbf{a}^{(1)}$ and the tensor $\mathbf{g}^{(1)}$.

$$\delta^{(1)} = \langle\mathbf{a}^{(1)}\mathbf{g}^{(1)}\rangle\frac{\mu_B S(S+1)}{3\hbar\gamma_I kT} = \langle\mathbf{a}^{(1)}\mathbf{g}^{(1)}\rangle\frac{\mu_B}{4\hbar\gamma_I kT} \tag{3}$$

where μ_B is the absolute value of the Bohr magneton and γ_I is the nuclear gyromagnetic ratio. Then, for a proton resonance, $\langle\mathbf{a}^{(1)}\mathbf{g}^{(1)}\rangle = b \times 253.54$ MHz. Similarly

$$\delta^{(2)} = 2\langle\mathbf{a}^{(2)}\mathbf{g}^{(2)}\rangle\frac{\mu_B}{\hbar\gamma_I\Delta\varepsilon_{ij}} \tag{4}$$

The only excited states that contribute significantly to $\delta^{(2)}$ occur at an energy $\Delta\varepsilon_{ij} = -(3/2)\zeta = -1425$ cm^{-1}, where ζ, the spin−orbit coupling constant, is taken to have a value (950 cm^{-1}) that fits the EPR data in a set of closely analogous compounds.[37] Equation 4 then gives $\langle\mathbf{a}^{(2)}\mathbf{g}^{(2)}\rangle = -\delta^{(2)} \times 7.361 \times 10^4$ MHz.

Figure 4a shows the temperature dependence of the axial and equatorial deuteration shifts of the Cp resonance in acetone-d_6 as well as in DMF-d_7 and nitromethane-d_3, whereas Figure 4b shows the corresponding Cp HSs of the fully protonated (H-15) pentamine complexes derived from the simulations. In order to emphasize the factor (close to −2) that relates the equatorial and axial deuteration shifts, the two vertical axes in Figure 4a are set so as to differ by a factor of 2. It has been assumed that the Cp resonance has no significant temperature dependence in the diamagnetic rhodium reference compound.

In order to attempt to extract the hyperfine coupling coefficients using eq 3, the EPR spectrum of **I** was measured in a 20% acetone-d_6/80% ethanol-d_6 glass at 7.5 K. It is broad. A simulation using an orthorhombic **g** tensor with principal components [2.2537, 2.0315, 1.7565] gives an excellent fit (SI, Figure S2). However, in solution there are only two (axial an equatorial) ^{1}H NMR ammine resonances (section 3.8); i.e., there is effective axial symmetry at the ruthenium center, and rotation of the asymmetric (η^5-C$_5$H$_5$)Fe(CO)$_2$ fragment about the bridging cyanide axis must be rapid. In the 7.5 K glass required to observe the EPR spectrum, this rotation is frozen out, and the asymmetry imposed on the π system of the cyanide bridge can remove its cylindrical symmetry. Density functional theory (DFT) calculations, although not quantitatively satisfactory, clearly show that the (η^5-C$_5$H$_5$)Fe(CO)$_2$CN fragment with an orientation fixed relative to the ruthenium pentamine group leads to both an orthorhombic splitting in the t_{2g} shell of the Ru^{III} ion [i.e., $E(d_{xz}) \neq E(d_{yz})$] and an orthorhombic **g** tensor. Unfortunately, the experimental **g** values cannot be attributed to particular molecular axes, so that explicit values of the hyperfine coupling coefficients could not be identified.

Table 4 therefore summarizes the composite observables $\langle\mathbf{a}^{(1)}\mathbf{g}^{(1)}\rangle$ and $\langle\mathbf{a}^{(2)}\mathbf{g}^{(2)}\rangle$ that can be extracted from Figure 4,
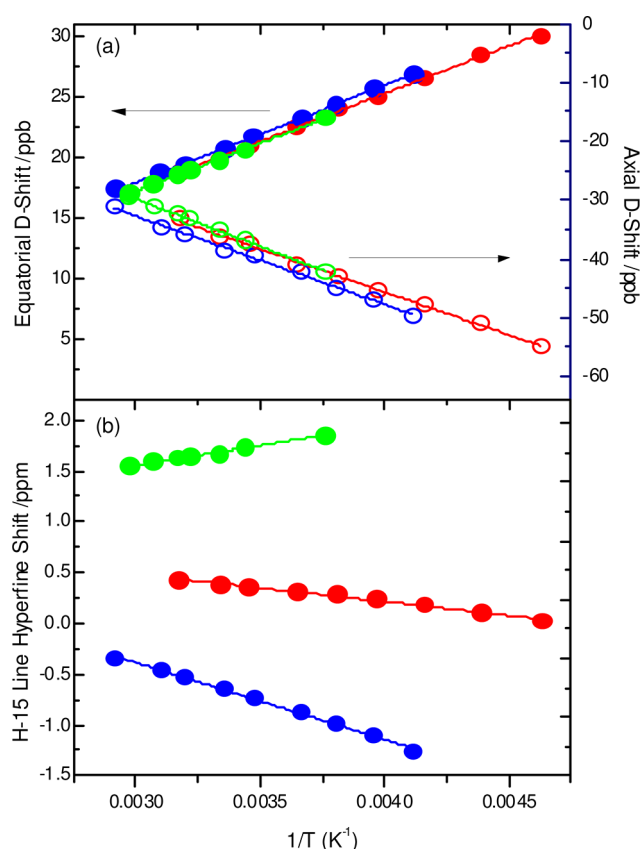
F

dx.doi.org/10.1021/ic400903a | *Inorg. Chem.* XXXX, XXX, XXX−XXX

Figure 4. Temperature dependence of (a) the deuteration shifts and (b) the HSs of the Cp protons of **I** in acetone-d_6 (red), DMF-d_7 (blue), and nitromethane-d_3 (green).

3.8. ^{13}C NMR and Ammine ^{1}H NMR. An isotopomeric structure is also observed in the Cp carbon peak in the ^{13}C NMR spectrum (125.7 MHz at 298 K) of a concentrated solution of **I** in acetone with 10.1% deuteration (SI, section S4 and Figure S4.1), which agrees well with the analogous ^{1}H NMR structure except that the equatorial and axial deuteration shifts are approximately twice as large (41 and −67.9 ppb, respectively), as are the line widths. The ^{13}C NMR spectrum is relatively noisy (due to a low natural abundance) and was resolution-enhanced. Because the instrument cryoprobe is optimized at 298 K, we have not studied the temperature dependence of the Cp carbon structure and so do not have parameters equivalent to those in Table 4. An isotopomeric structure was not observed in the broad ^{13}C cyanide resonance (fwhm ~1700 Hz).

The chemical shifts of the broad ammine proton resonances (fwhm ~1500 Hz at 500 MHz) in compound **I** vary widely in different solvents. The chemical shifts are listed (SI, section S3) and plotted in Figure 5a against the Cp HS in the same solvent. In an aqueous solution, deuteration isotopomers can be identified in the axial and equatorial proton ammine resonances (SI, Figure S3.1) with judicious use of resolution enhancement.

Figure 5b plots the difference between the axial and equatorial resonances against the Cp HS. In the 95% D_2O solution, the residual protons are predominantly present in the (3,11), (3,10), (2,12), and (2,11) species and the weighted mean of the Cp HS has been used. The linear correlations in both parts of this figure are excellent. Figure 5a implies that a suitable solvent mixture should give a single degenerate ammine resonance at 155.6 ppm with a corresponding small Cp HS of +0.121 ppm. For comparison, a single ammine proton resonance has been observed for the octahedral $Ru(NH_3)_6{}^{3+}$ ion in nonaqueous aprotic solvents[35] at ~156 ppm (500 MHz; ~300 K). Similarly here, an acidified aqueous solution with a proton/deuterium ratio of 95:5 displays the resonance at 157.1 ppm (950 MHz; 298 K). These observations illustrate the presence of a large contact contribution to the HS in the ammine proton resonances. (When the small temperature difference between the non-aqueous data at 500 MHz (300 K) and the aqueous data at 950 MHz (298 K) is taken into account, the hexaammine signal at 300 K is closer to 156.7 ppm.) When the axial and equatorial ammine resonances are degenerate, the spin density distribution in the t_{2g} orbitals of **I** is close to isotropic and comparable to that in the hexaammine, and at this point, any Cp HS is small compared to those typically observed in common solvents.

We have recently shown that the differential shift in the axial and equatorial ammine resonances of the related compound $[(CO)_5Cr(\mu\text{-CN})Ru(NH_3)_5](CF_3SO_3)_2$ in the same five

together with their standard errors. The values associated with deuteration indicate the changes in $\langle\mathbf{a}^{(1)}\mathbf{g}^{(1)}\rangle$ and $\langle\mathbf{a}^{(2)}\mathbf{g}^{(2)}\rangle$ introduced by the replacement of NH_3 by NH_2D in either the axial or equatorial ammine ligands.

Figure 4 and Table 4 show that an axial deuteration has almost twice the influence in the opposite sense to an equatorial substitution and that this applies to both the temperature-dependent and -independent components of the shift. Notice that, whereas changes introduced by deuteration are almost independent of the solvent, this is not true of the absolute value of the Cp HS. The HSs (Figure 4b) are adequately described by a linear dependence on $1/T$, from which the parameters in Table 4 are drawn. However, there is a small nonlinear contribution that is most obvious in acetone solutions. The implication is that solvation of the complex is not quite independent of temperature (section 4.8).

Table 4. Cp Proton HSs and Coupling Parameters

| hyperfine/D shift	solvent	$\delta^{(1)}/10^{-9}$ (298 K)	$\langle\mathbf{a}^{(1)}\mathbf{g}^{(1)}\rangle$/kHz	$\delta^{(2)}/10^{-9}$	$\langle\mathbf{a}^{(2)}\mathbf{g}^{(2)}\rangle$/kHz
HS (H-15 resonance)	DMF	−2540 ± 40	−191 ± 3	1885 ± 50	−138 ± 3
	acetone	−908 ± 40	−68 ± 3	1296 ± 40	−95 ± 3
	nitromethane	1310 ± 130	100 ± 10	379 ± 50	−28 ± 4
axial ammine (deuteration shift)	DMF	−50.3 ± 1.1	−3.80 ± 0.09	12.2 ± 1.2	−0.85 ± 0.08
	acetone	−47.6 ± 0.8	−3.71 ± 0.06	12.8 ± 0.9	−0.90 ± 0.06
	nitromethane	−54.2 ± 0.6	−4.09 ± 0.05	18.6 ± 0.8	−1.37 ± 0.06
equatorial ammine (deuteration shift)	DMF	26.8 ± 0.2	2.02 ± 0.02	−6.1 ± 0.3	0.42 ± 0.02
	acetone	26.4 ± 0.4	1.99 ± 0.04	−6.2 ± 0.6	0.44 ± 0.04
	nitromethane	26.4 ± 0.2	1.99 ± 0.02	−6.4 ± 0.3	0.47 ± 0.02
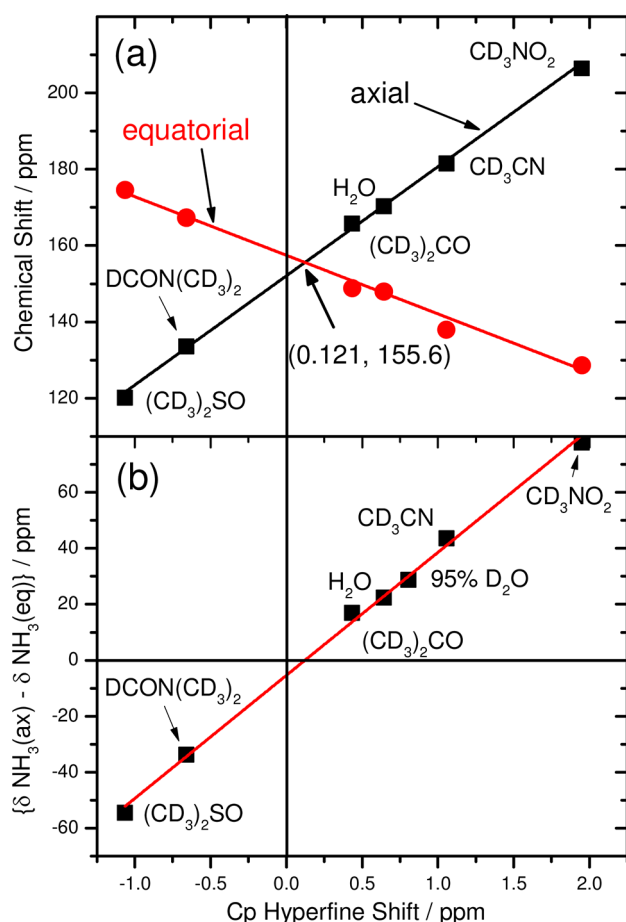
Figure 5. (a) Axial (black) and equatorial (red) ammine chemical shifts and (b) the axial–equatorial shift difference versus the Cp HS in various solvents (500 MHz; 300 K).

organic solvents can, as a first approximation, be linearly correlated ($R^2 = 0.979$) with the energy of the metal-to-metal charge-transfer (MMCT) transitions that are characteristic of this family of mixed-valence compounds.[38] The charge-transfer energies in seven solvents that include the five organic solvents in Figure 5 are, in turn, linearly correlated ($R^2 = 0.995$) with the solvent donor strength, as quantified by the Gutmann donor number,[39,40] a parameter derived from the heat of formation of SbCl$_5$ adducts, that, in this context, reflects the strength of the hydrogen-bonding interaction between the solvent and ammine groups. Both the Cp HS and the difference in the axial and equatorial ammine shifts are thus directly proportional to the solvent donor number.

The slopes of the axial and equatorial plots in Figure 5a are +28.6 and −15.36, respectively. The factor close to −2 between these figures suggests that deviations from the shift in the isotropic case arise from the influence of the tetragonal field on the spin density distribution between the d_{xy} and $d_{xz,yz}$ orbitals (vide infra).

3.9. Optical Absorption. The Hush model,[41] although crude, allows the extent of charge transfer between the nominally diamagnetic iron and paramagnetic ruthenium atoms to be estimated from the energy and integrated intensity of the MMCT transition. Although the MMCT band in **I** is solvatochromic, in acetone the transition is at 21965 cm^{-1}, with $\varepsilon_{max} = 1160$ mol^{-1} dm^3 cm^{-1} and a fwhm bandwidth of ~5320 cm^{-1}, from which the weight of the charge-transfer

configuration in the ground state (conventionally denoted by α^2) can be calculated as 0.47%; this figure can be used as a rough indicator of the magnitude of the spin density on the iron atom. In a comparison of the optical spectrum of **I** in 100% D$_2$O and 100% H$_2$O, the effects of deuteration do not show any significant changes in the MMCT absorption ($\lambda_{max} \sim 21600$ cm^{-1}; $\varepsilon_{max} \sim 1130$ mol^{-1} dm^3 cm^{-1}; $\alpha^2 \sim 0.45\%$); the profile is too broad. The spin density located on the bridging atoms, which DFT calculations suggest can be substantial,[2] as well as that distributed onto auxiliary ligands bound to the iron atom is ignored in this treatment. Moreover, only a portion of the spin on the ruthenium atom is in the $4d_{xz}$ and $4d_{yz}$ orbitals with the correct symmetry to interact with the bridge.[2]

3.10. Computational Estimate of the Contact Interaction. An approximate description of the first-order contact part of the Cp HS was sought using DFT calculations, based on two geometry optimizations of the gas-phase cation undertaken using the Gaussian code. One of these is constrained to C_s symmetry and closely resembles the geometry found in the crystal structure (Figure 1), while in the other, no symmetry constraints were applied, yielding a computed structure in which the ammine–ruthenium bonds are eclipsed with respect to the iron–carbonyl bonds. ADF calculations incorporating the spin–orbit interaction indicate that these two structures do not differ significantly in their total energy or in their bond lengths or angles, which are in agreement with the experimental values. Calculations were made both in the gas phase and in various solvents, with the solvation being modeled by the COSMO method. Explicit solvation was also modeled by attaching five H$_2$O molecules, each hydrogen-bonded to an ammine ligand. Calculation of the spin density used ZORA and excluded the spin–orbit interaction. Inclusion of the spin–orbit interaction enabled **g** values and hyperfine coupling coefficients to be estimated. Spin densities, derived from Mulliken populations, are available from the ZORA method but not from the spin–orbit calculation because the spin projection operator does not have defined eigenvalues.

The results in all cases indicate a large spin density on iron (from 5% to 19%), which is not consistent with the Hush model (~0.5%, section 3.9). However, DFT calculations have a well-known limitation when applied to molecules with extensive charge transfer. In practice, the inexact treatment of the electron self-interaction leads to unrealistically low excitation energies for charge-transfer states and an unrealistically large degree of charge transfer in the ground state.[42] For example, the first MMCT transition in the $[(CN)_5Ru(\mu\text{-}CN)Ru(NH_3)_5]^-$ anion, which has an electronic structure similar to that of **I**, is computed to occur at 1.0 eV, whereas experimentally it is found at 1.8 eV.[43] Also, the extent of spin transfer is strongly dependent on the choice of the functional. For example, the spin density on the iron atom in the gas phase was computed to be 45% using the BP functional but 27% using the B3LYP hybrid functional. In an optimized solvated geometry in which five water molecules are bound to the ammine groups, the spin density (using B3LYP) on iron drops to 5%.

Finally, the inclusion of the spin–orbit interaction stabilizes the configuration in which the unpaired spin is localized on the ruthenium atom rather than the iron atom. Thus, in a ZORA calculation, the charges on the ruthenium and iron atoms are +1.38 and −0.20, respectively, whereas the inclusion of the spin–orbit interaction yields values of +1.20 and −0.46, respectively. The reduced positive charge on the ruthenium

H

dx.doi.org/10.1021/ic400903a | *Inorg. Chem.* XXXX, XXX, XXX–XXX

atom is consistent with an increase in the positive charge on the ammine nitrogen atoms due to the spin−orbit stabilization of the Ru^{III} 4d shell, whereas the increased negative charge on the iron atom indicates a reduction in the extent of (negative) charge transfer due to the loss of this stabilization in the charge-transfer configuration.

Against this background, it is clear that DFT calculations are not a reliable tool for determining the absolute extent of spin transfer nor is the COSMO model realistic in this class of molecules because explicit solvent interactions with the acidic ammine protons strongly influence the degree of charge transfer, a result that has long been established experimentally. Nevertheless, the distribution of the spin density between the iron atom and the Cp protons, if appropriately scaled to account for excessive spin transfer from the ruthenium center, should be an indication of the magnitude and sign of the isotropic (contact) component of the HS. So, for example, the average of the calculated isotropic shifts for the five Cp protons in an aqueous COSMO model, averaged over the two geometries discussed above, yields a hyperfine coupling constant a_H of 0.063 MHz (SI, Table S7.4). This corresponds to a positive HS at room temperature (assuming $g = 2$) of $\delta_h = 1.68$ ppm and is derived using a functional that gives a spin density of 18% on the iron atom in a ZORA calculation. Scaling this result to the Hush estimate of a ~0.5% spin density on iron, we anticipate that the contact contribution to the Cp proton hyperfine coupling constant would be ~1.8 kHz, thus about 2 orders of magnitude smaller than the values reported in Table 4.

Table S7.4 in the SI also contains the results for the ^{13}C hyperfine coupling constants, with the aqueous solution average being 0.264 MHz; that is, they are predicted to be a factor of 4.1 large than those for the Cp protons, a ratio similar to that computed for the gas-phase ions. Similar scaling, using the Hush estimates, suggests a ^{13}C contact contribution of ~7.5 kHz.

4. DISCUSSION

4.1. The Hyperfine Coupling Mechanism. The Cp proton HS comprises Fermi contact and dipolar (pseudocontact) contributions. In this section, we seek to establish their relative importance. In section 3.10, DFT calculations were used to estimate the contact part of the hyperfine coupling constant (a_H), and using that value in

$$\delta_c = \frac{a_H}{\hbar} \frac{g\mu_B S(S+1)}{3\gamma_I kT} \tag{5}$$

the temperature-dependent part of the HS at room temperature is predicted to be on the order of +45 ppb. This is 1 or 2 orders of magnitude smaller than the experimental values in Table 4 (which range from +1.3 to −2.5 ppm) and therefore cannot account for the main features of our observations. A similar argument can be applied to the Cp ^{13}C data, although the relatively large deuteration shifts imply that the contact interaction at the carbon nucleus may not be negligible. On the other hand, the Cp proton pseudocontact shift due to a first-order electronic moment centered on the ruthenium is given by[44]

$$\delta_{pc} = \frac{\mu_0}{4\pi} \frac{\mu_B^2 S(S+1)}{9kT} (g_\parallel^2 - g_\perp^2) \left(\frac{3\cos^2\theta - 1}{r^3} \right) \tag{6}$$

The geometric factor in the final bracket, when averaged for rotation about the Fe−Cp axis, is 6.434×10^{27} m^{-3}, from which we compute that, at room temperature

$$\delta_{pc} = 1.12 \times 10^{-6}(g_\parallel^2 - g_\perp^2)$$

Typical values of the HS then require $g_\parallel^2 - g_\perp^2 \sim 1$, which is smaller than the values found by EPR for the analogue $[(CO)_5Cr(\mu\text{-}CN)Ru(NH_3)_5]^{2+}$ in which the charge transfer is significantly larger.[2] The pseudocontact mechanism is therefore a realistic source of the HS in **I**.

4.2. Evidence for a Predominant Pseudocontact Mechanism. The degree of charge transfer, estimated in section 3.9,[39] controls the extent of spin transfer across the bridge and, therefore, the magnitude of any contact part of the Cp HS. Strong donor solvents raise the energy of the vacant metal(III) ammine orbitals, thereby increasing the MMCT energies and reducing the extent of charge transfer. The positive contact shift computed in section 3.10 should therefore be smaller in DMF than in nitromethane. Similarly, the temperature dependence of the shift should be negative and at its largest in nitromethane. Both predictions are the opposite of what is observed.

Modification of the Ru^{III}−bridge interactions that accompany changes in solvation influences the tetragonal field parameter as well as the **g**-value anisotropy (vide infra). EPR measurements on an analogous compound in frozen glasses show that $g_\parallel^2 - g_\perp^2$ is much more positive in a nitromethane solution than in DMF.[2] The source of this anisotropy lies in the relative ordering of the d_{xy} and $d_{xz,yz}$ orbitals and is determined by the interaction of the latter pair with the π orbitals of the bridge. To the extent that the d^5 hole occupies $d_{xz,yz}$, the axial orbital contribution to the magnetic moment is enhanced and $g_\parallel$ increases relative to $g_\perp$. The consequences should therefore be a larger downfield temperature-dependent HS in nitromethane than in DMF, in agreement with the data in Table 2.

A clear signature of the pseudocontact mechanism can be found in Figure 5b, which shows that the Cp HS and the differential shift of the axial and equatorial ammine protons in various solvents, including measurements in 100% H_2O and 95% D_2O, are strongly linearly correlated (coefficient of determination $R^2 = 0.9931$). The significant feature of Figure 5b is the small residual Cp HS predicted when the axial and equatorial ammine resonances are degenerate. Because the equatorial and axial Ru−N distances are almost identical (Table 1), the spin density in the 4d orbitals, under these conditions, must be close to isotropic and the large contact shifts experienced by the ammine protons must also be nearly equal. Furthermore, the ruthenium-centered contribution to the **g**-tensor anisotropy, and therefore (from eq 6) the Cp HS, must both be close to zero.

We do not have sufficient evidence to identify the origin of the small residual Cp HS when the ammine resonances are degenerate. However, the interaction of d_{xz} and d_{yz} with the π orbitals of the bridge ensures that some of the spin density contributing to $g_\parallel$ is closer to the Cp ring than that centered on the ruthenium atom. While the HS of the ammine protons is most sensitive to the spin density localized on ruthenium, any density on the bridge will, according to eq 6, make a positive contribution to the Cp HS, matching the observed results.

4.3. Deuteration Shifts. Figure 4a shows that the small Cp HSs arising from a single deuteration are almost identical in the three solvents despite their very different donor properties.

J

dx.doi.org/10.1021/ic400903a | *Inorg. Chem.* XXXX, XXX, XXX–XXX

Because the extent of charge (and spin) transfer is strongly dependent on these differences in solvation, any change in a contact contribution, stemming from the spin redistribution between the t_{2g} orbitals induced by an ammine deuteration, would be expected to be strongly solvent-dependent. Its absence is therefore another strong indicator that the effects of deuteration are not manifest via the contact mechanism but by the pseudocontact mechanism.

The overall downfield shift in the Cp resonance of 152 ppb associated with the presence of an average of 12.6 ammine deuterium atoms in the first coordination sphere (Figure 2) is much larger than the ~20 ppb downfield shift of the H-15 species between 100% H_2O and 100% D_2O solutions (δ_0 in Table 2) attributable to differential outer-sphere solvation. Figure 4a also shows that deuteration in the equatorial ammine ligands introduces a positive contribution to the temperature-dependent part of the Cp HS ($\delta^{(1)}$). Its effect is therefore analogous to that shown by the H-15 HS in Figure 4b upon switching from DMF to nitromethane, in which the change in the donor properties of the solvent is the average of its effect on the four equatorial ammines and the single axial ammine. It follows that deuteration in a single ammine ligand makes it a weaker donor and the ruthenium ion a better acceptor.

4.4. Sign of the Deuteration Shift and Hyperconjugation. The conclusion that ND_3 is a *weaker* donor than NH_3 could be due to a change in either the σ or π interactions with the metal ion. Two long-standing observations indicate that ND_3 is actually a *stronger σ donor* than NH_3.

The optical absorption spectra of single crystals of [Co-$(NH_3)_6$][Ir(CN)$_6$] and [Co(ND_3)$_6$][Ir(CN)$_6$] at 4.2 K show a resolved vibronic structure, from which it may be inferred that the pure electronic $^1A_{1g} \rightarrow {}^1T_{1g}$ transition of Co^{III}, which is found near 18380 cm^{-1} in the protonated compound, shifts by ~80 cm^{-1} to higher energy in the deuterated analogue.[45] Because the $t_{2g} \rightarrow e_g$ (d–d) excitation energy responsible for this transition is dominated by σ-antibonding interactions, it follows that ND_3 is the stronger σ donor.

The same conclusion can be drawn from the H/D isotopomeric structure in the ^{59}Co NMR spectra of diamagnetic Co(en)$_3$Cl$_3$ in H_2O/D_2O mixtures.[46] In the ^{59}Co NMR spectrum of Co(NH_3)$_6$Cl$_3$, the D-18 species is found to be 93.6 ppm upfield of that in the H-18 species. Many years ago, in a classic paper by Freeman, Murray, and Richards,[47] the ^{59}Co chemical shifts of a large number of spin-paired Co^{III} d^6 compounds were shown to include a temperature-independent paramagnetic contribution that is linearly related ($R^2 = 0.992$) to the wavelength of the first d–d transition. Using the slope of that relationship, the shift of 80 cm^{-1} in the optical transition of Co(NH_3)$_6$Cl$_3$, as a result of full deuteration, predicts an upfield shift of 99.0 ppm in the ^{59}Co resonance, in good agreement with that observed in the optical spectrum.[46]

In summary, ND_3 is a stronger σ donor than NH_3. However, the unpaired spin density in a low-spin Ru^{3+} d^5 ion is present in the $t_{2g}(d_\pi)$ orbitals, so the hyperfine coupling marks a change in the covalency of the metal–ligand π interactions and the importance of hyperconjugation. This long-established concept in organic chemistry implies that nitrogen and hydrogen atomic orbitals, nominally associated with a localized N–H σ bond, also contribute to molecular orbitals involved in the N–Ru π bond. It follows from the downfield shift of the Cp resonances in compound **I**, taken with the trend shown in Figure 4, that ND_3 is a *weaker π donor*. Similar effects occur in methyl hyperconjugation. For example, the ^{13}C NMR spectra of

toluene-α-d_3 show a downfield shift that is large at C-4 and smaller at C-2 and C-6, while there is no shift C-3, implying that CD_3 is a weaker π donor than CH_3.[48] NMR studies of deuterium isotope shifts in methyl-substituted carbocations reach the same conclusion.[49−51] Finally, we note that the upfield HS of the resonance of the fully protonated impurity species containing one coordinated water molecule (section 3.4) also supports this analysis (SI, section S1).

We conclude that deuteration in the equatorial ammines lowers the energy of the $d_{xy}(\equiv t_2^0)$ orbital relative to those of $d_{xy,yz}(\equiv t_2^{\pm1})$, making the tetragonal field parameter ν (defined by $\langle t_2^0|Y_2^0|t_2^0 \rangle = \nu$ and $\langle t_2^{\pm1}|Y_2^0|t_2^{\pm1} \rangle = -^1/_2\nu$) more negative, while the reverse is true for an axial substitution. Thus, a positive increase in ν leads to a decrease in the Cp HS. Expressed in this way, it is easy to see why the effect of an axial ammine deuteration is of opposite sign and twice as large as the effect of an equatorial ammine deuteration. Apparently, the Cp HS is due to a pseudocontact mechanism, with a magnitude determined by the tetragonal field parameter.

4.5. Empirical Model of the HSs. A more detailed treatment of what follows can be found in section S6 in the SI. The $^2T_{2g}$ ground state of the low-spin octahedral Ru^{3+}(d^5) ion is split by the spin–orbit interaction ($\zeta \sim 950$ cm^{-1}) into two sets of levels, which, in O* double-group representations, are an E'' Kramers doublet ground state and an excited U' quartet. Their separation is $^3/_2\zeta \approx 1425$ cm^{-1}, which means that the thermal population of the U' state is negligible at ambient temperature (~0.2%). Symmetry-determined coupling constants[52] establish that the electronic wave functions can be written as

$$|E''\alpha''\rangle = \frac{1}{\sqrt{3}}|T_2^0, \alpha'\rangle - \frac{\sqrt{2}}{\sqrt{3}}|T_2^1, \beta'\rangle$$

$$|E''\beta''\rangle = -\frac{1}{\sqrt{3}}|T_2^0, \beta'\rangle + \frac{\sqrt{2}}{\sqrt{3}}|T_2^{-1}, \alpha'\rangle$$

$$|U'\kappa\rangle = -\frac{1}{\sqrt{3}}|T_2^{-1}, \alpha'\rangle - \frac{\sqrt{2}}{\sqrt{3}}|T_2^0, \beta'\rangle$$

$$|U'\nu\rangle = -\frac{1}{\sqrt{3}}|T_2^1, \beta'\rangle - \frac{\sqrt{2}}{\sqrt{3}}|T_2^0, \alpha'\rangle$$

$$|U'\lambda\rangle = |T_2^{-1}, \beta'\rangle$$

$$|U'\mu\rangle = |T_2^1, \alpha'\rangle \tag{7}$$

where α' and β' are spin functions with $m_s = +^1/_2$ and $-^1/_2$, respectively. We adopt a contracted notation in which the ground-state components are labeled by $i = \alpha, \beta$ and those of the U' excited-state quartet by $j = \kappa, \lambda, \mu, \nu$. In the cyanide-bridged ruthenium(III) pentaammine complexes, the tetragonal component of the ligand field introduces a first-order splitting of the U' quartet, while also mixing α with ν and β with κ. The T_2^0 and $T_2^{\pm1}$ functions of eq 7 are associated with holes in the d_{xy} and $d_{xy,yz}$ orbitals, respectively. Only the spin in the latter pair can be transferred across the cyanide bridge.

It is convenient to define the tetragonal field at the Ru^{III} center, relative to the spin–orbit coupling constant, by a dimensionless parameter $t = \nu/\zeta$ (please note a change of notation from SI, section S6, where $x \equiv t$). Simple expressions for the contact and pseudocontact shifts linear in t can then be derived when $t \ll 1$, a realistic approximation in the current compound. We also assume that the magnetic moment matrix
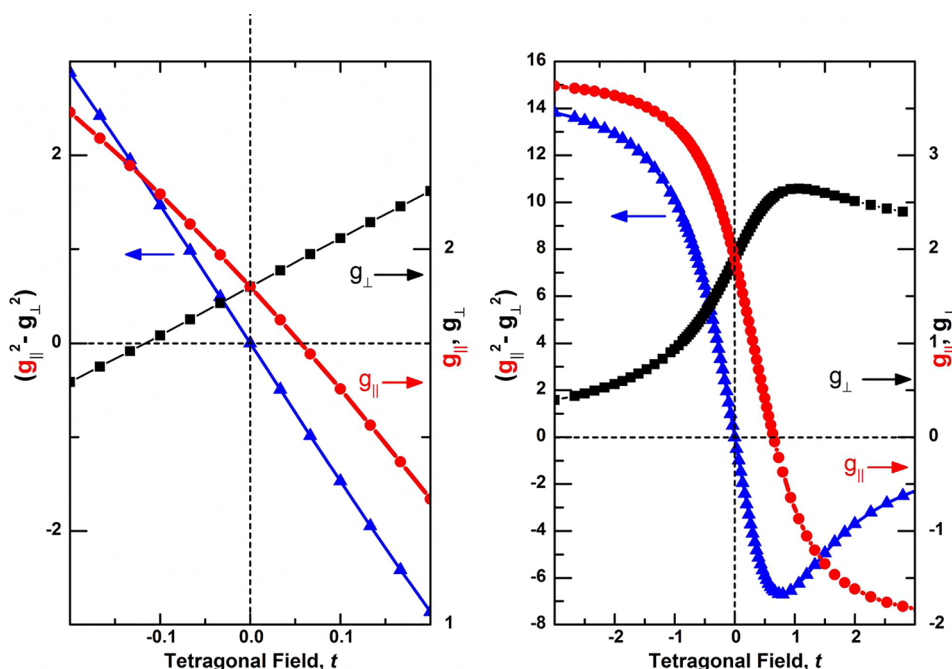
Figure 6. Functions of the **g** tensor versus dimensionless tetragonal field parameter t ($t = \nu/\zeta$): (right) $g_\parallel$ (red) and $g_\perp$ (black); (left scale) $g_\parallel^2 - g_\perp^2$ (blue). The figure to the right is over a wider range of t.

elements are adequately approximated by employing a 4d t_{2g} basis, an approximation whose validity is supported by the small extent of charge transfer indicated by the Hush model.

4.6. Contact (Isotropic) Shifts. The Fermi contact term (SI, section S6) leads to an expression for the HS

$$\delta_c = \frac{\mu_0 g_e \beta}{9} \sum_{k=x,y,z} \sum_{i=\alpha,\beta} \left[2 \sum_j \frac{\langle i|\hat{\mu}_k|j\rangle \langle j|\sum_n \delta(\mathbf{r}_n)\hat{s}_k|i\rangle}{\Delta\varepsilon_{ij}} \right.$$
$$\left. - (kT)^{-1}\{\langle i|\hat{\mu}_k|i\rangle \langle i| \sum_n \delta(\mathbf{r}_n)\hat{s}_k|i\rangle\} \right] \tag{8}$$

where $\mathbf{r}_n$ is the nuclear position vector. The evaluation of this expression requires the spin density at the NMR nucleus, defined by $\rho_s(r_n) = 2\sum_n \delta(\mathbf{r}_n)\hat{s}_k$. Following Kurland and McGarvey,[36] we assume that it is linearly related to the spin-angular momentum evaluated at the metal center, via coupling coefficient K_m, which quantifies the extent of delocalization of the spin away from the ruthenium ion, as well as the spin polarization in the region of the nucleus. In other words, $K_m = \delta(\mathbf{r}_n)_m = \langle T_2 \pm m(\mathbf{r}_n)|T_2 \pm m(\mathbf{r}_n)\rangle$.

For the ammine protons in **I**, it is assumed that the coupling coefficients describing the contact interaction with spin in the d_{xy} and $d_{xy,yz}$ orbitals are equal, i.e., $K_0 = K_1$, although there is, of course, no requirement for the spin density in these orbitals to be equal. We then obtain, for protons in the axial and equatorial ammine ligands, respectively

$$\delta_c(\text{ax}) = \frac{\mu_0 g_e \beta^2 K_1}{9}\left[2\left(\frac{16}{9\zeta} + \frac{1}{3kT} - \frac{4t}{27\zeta} - \frac{2t}{3kT}\right)\right] \tag{9a}$$

$$\delta_c(\text{eq}) = \frac{\mu_0 g_e \beta^2 K_1}{9}\left[2\left(\frac{16}{9\zeta} + \frac{1}{3kT} + \frac{2t}{27\zeta} + \frac{t}{3kT}\right)\right] \tag{9b}$$

In the case of the Cp protons, the ligand is bound to the iron atom, and only spin originating in the Ru d_{xy} and d_{yz} orbitals by transmission through the cyanide bridge will generate a contact shift, in which case eq 9a is appropriate, although K_1 is obviously smaller than that applicable to the ammine protons. When $t \ll 1$, the first two terms in eqs 9a and 9b, which arise from the spin distribution in the Ru 4d orbitals in an octahedral field, should make a much larger contribution to the contact shift than that afforded by the tetragonal field. Any variations attributable to changes in solvation are then most naturally ascribed to changes in the overall extent of charge and spin transfer and will be reflected in the value of the coupling coefficients K_1. However, eq 9a also implies that the effect of solvation on K_1 will also be manifested in any tetragonal field contribution and the changes in it introduced by deuteration.

When $t \sim 0$, the pseudocontact contribution to the ammine proton HS should be absent (see eq 11), while eq 9 implies that the axial and equatorial ammine contact contributions will be equal. Nevertheless, eq 9 also predicts a large contact contribution to the HS in the Cp protons. However, Figure 5b makes it clear that, in the case where the axial and equatorial ammine HSs are equal, the Cp proton HS is close to zero. It follows that the contact contribution must be small and insignificant compared to the pseudocontact contribution.

4.7. Pseudocontact Shifts. Assuming that the main dipolar contribution to the HS is the ruthenium-centered electronic moment in a site of axial/tetragonal symmetry, the temperature-dependent part of the shift is given by[44]

$$\delta_{pc}^{(1)} = \frac{\mu_0}{4\pi}\frac{\beta^2}{12kT}(g_{zz}^2 - g_{xx}^2)\frac{1}{r^3}(3\cos^2\theta - 1) \tag{10}$$

Within the 4d orbital basis, the **g**-tensor anisotropy is easily expressed (SI, section S6) in terms of t, so that

$$\delta_{pc} = \frac{\mu_0}{4\pi}\frac{(3\cos^2\theta - 1)\beta^2}{3r^3}\left\{\frac{8t}{3\zeta} - \frac{4t}{kT}\right\} \tag{11}$$

Comparing eqs 10 and 11 (with $t \ll 1$) leads to $g_{zz}^2 - g_{xx}^2 \equiv g_{\parallel}^2 - g_{\perp}^2 = -16t$.

To avoid the approximation imposed by $t \ll 1$, a Hamiltonian using the states in eq 7 as bases was diagonalized for several values of t, using an orbital reduction factor of 0.925 that was found to be appropriate in earlier work.[2] The g values are derived from the eigenvectors. Figure 6 shows that $g_{zz} \equiv g_{\parallel}$, $g_{xx} \equiv g_{\perp}$, and $g_{\parallel}^2 - g_{\perp}^2$ are each effectively linear with respect to t provided that $-0.2 < t < 0.2$ (Figure 6 at the right shows how deviations from linearity occur for larger values of $|t|$).

Fitting the data in Figure 6a for $g_{\parallel}^2 - g_{\perp}^2$ versus t, where $-0.2 < t < 0.2$, leads to the simple expression $g_{\parallel}^2 - g_{\perp}^2 \equiv -14.6t$. The small difference between this result and that derived from eqs 10 and 11 comes partly from the simplifying assumptions used in the derivation of eq 11 (SI, section S6), such as neglect of the first-order tetragonal field splitting of the U' excited states, and partly from the influence of the orbital reduction factor. Equation 10 then allows the value of t to be deduced from the HS.

Using eq 10 together with $g_{\parallel}^2 - g_{\perp}^2 = -14.6t$ and the geometric factor computed previously, we find that at room temperature

$$\delta_{pc}^{(1)} = -1.635 \times 10^{-5}t \tag{12}$$

A comparison with the values of $\delta^{(1)}$ in Table 4 yields $t = +0.155$, $+0.055$, and -0.080 in DMF, acetone, and nitromethane, respectively, so that the tetragonal field parameter ν takes the values $+147$, $+52$, and -76 cm^{-1}, respectively. These results are relatively insensitive to the change in the solvent compared to those obtained from the EPR of frozen solutions of $[(OC)_5Cr(\mu\text{-}CN)Ru(NH_3)_5](PF_6)_2$. In the latter compound, a larger degree of charge transfer, inferred from the optical spectrum, predicts larger differences in the tetragonal field, so that $\nu = -1257$ cm^{-1} in nitromethane and -112.5 cm^{-1} in DMF.

These relationships can be used to show that the change in the tetragonal field due to a single deuteration in the axial ammine is $+2.8$ cm^{-1} and that in the equatorial ammine is -1.5 cm^{-1}. The linear relationship between $g_{\parallel}^2 - g_{\perp}^2$ and t in Figure 6a also allows us to write $\Delta\delta^{(1)} = (d\delta^{(1)}/dt)\Delta t = -1.635 \times 10^{-5}\Delta t$, where Δt is, for example, the small change in the tetragonal field associated with ammine deuteration. This relationship is independent of the absolute value of t and accounts for the invariance of the deuteration shifts in Figure 4 and Table 4 despite t varying significantly between the three different solvents.

There are two mechanisms by which t responds to modifications in the ammine ligands. On the one hand, the results of deuteration appear directly via hyperconjugation as energy differences between the d_{xy} and $d_{xy,yz}$ orbitals. On the other hand, any decrease in the donor properties of the ammine, as illustrated by the effect of the solvents of different donicity, lowers the mean energy of the Ru t_{2g} orbitals closer toward the π-bonding orbitals of the bridge and increases the interaction energy of the $d_{xy,yz}$ orbitals with it. Their energies are therefore raised relative to d_{xy}, so that the Cp resonance experiences a downfield shift. We suggest that this lowering of the mean energy of the t_{2g} orbitals is why axial deuteration leads to a change in the HS (typically -37 ppb) that is less negative than twice the change induced by deuteration in an equatorial ammine of $+20$ ppb (Table 3). The observed values would then comprise a common shift of $+1$ ppb taken with equatorial and axial shifts of $+19$ and -38 ppb, respectively.

Finally, we note that a comparison of ^{1}H and ^{13}C Cp deuteration shifts allows us to estimate the relative importance of the pseudocontact and contact contributions. The ^{13}C shifts are of the same sign as those in the proton case but are almost twice as large in the ^{13}C NMR spectrum. The geometric factor in the pseudocontact contributions is 1.2 times larger in the ^{13}C case, and according to the calculations in Table S7.4 in the SI, the contact contribution is predicted to be larger by a factor of 4.1. It is then simple to deduce that the relative importance of the pseudocontact and contact contributions in the proton spectrum is in the ratio of 2.65:1, justifying the basis for our previous analysis. There are, of course, uncertainties in this result, largely attributable to extrapolation from the DFT results.

4.8. First- and Second-Order Contributions to Hyperfine Interaction. If the change in the Cp HS, $\Delta\delta$, caused by deuteration is attributable to a change in the tetragonal field, Δt, then eq 11 indicates that the two contributions to the pseudocontact interaction are related by

$$\Delta\delta_{pc}^{(1)} = -\frac{3\zeta}{2kT}\Delta\delta_{pc}^{(2)} \tag{13}$$

Taking $\zeta = 950$ cm^{-1}, then at 298 K eq 13 predicts $\Delta\delta_{pc}^{(1)} = -6.88\Delta\delta_{pc}^{(2)}$. In Table 4, the experimental relationship is close to $\Delta\delta_{pc}^{(1)} = -4.2\Delta\delta_{pc}^{(2)}$. The magnitude and sign of the experimental relationship between the two contributions broadly support the assumptions made in deriving eq 11, although we are unable currently to account for the quantitative discrepancy. We note, however, from eq 9a that in any contact contribution $\Delta\delta^{(1)}$ and $\Delta\delta^{(2)}$ should have the *same* sign rather than the opposite signs in eq 13, moving the result closer to that observed experimentally.

The relationship between the two components $\Delta\delta^{(1)}$ and $\Delta\delta^{(2)}$ of the overall HS in Table 4 is less clear-cut. The experimental $\Delta\delta^{(2)}$ values are derived from a long extrapolation of the linear relationship used to obtain $\Delta\delta^{(1)}$. However, the $1/T$ dependence of δ contains a significant quadratic component, such that the slope increases with $1/T$, particularly in acetone and DMF (section 3.7). We attribute this to an increase in the magnitude of the ammine–solvent interaction with decreasing temperature that enhances the tetragonal field perturbation responsible for the HS. Two further observations support this conclusion: (i) Upon freezing an acetone solution of **I**, the orange solution becomes yellow, signifying an increase in the MMCT energy due to an increase in the effective donor number of the medium. (ii) In acetone at room temperature, the axial ammine shift is greater than the equatorial shift (Figures 5), but these resonances converge and coalesce at -60 °C, indicating an isotropic environment. This additional source of temperature dependence invalidates the extrapolation used to obtain the $\Delta\delta^{(2)}$ values in Table 4, meaning that these are not readily amenable to interpretation.

4.9. Spectral Line Widths. The visibility and analysis of the myriad of isotopomer resonances discussed in this work rely on their spectral narrowness. An application of the Solomon equations, based on dipole–dipole relaxation, the geometry of complex **I** giving $\langle 1/r^3 \rangle^2 = 2.19 \times 10^{55}$ m^{-6}, and the electron correlation time of 10^{-11} s reported for Ru(NH$_3$)$_6^{3+}$ predicts a fwhm line width of 6.04 Hz, in close agreement with experiment (6.2 at 500 MHz). This strongly

supports the assertion that the dipolar interaction is the main source of hyperfine interaction.

Figure 7 compares the 950 MHz spectrum of compound **I** in acetone-d_6 with that of $[(\eta^5\text{-}C_5H_5)Ru(CO)_2(\mu\text{-CN})Ru\text{-}$

Figure 7. 950 MHz ^1H NMR spectra of the Cp resonance in acetone-d_6 of (a) **I** and (b) **II**. Both plots span 0.25 ppm, but the horizontal axes are offest so that the strongest resonances coincide. The plot colors are as in Figures 2 and 3.

$(NH_3)_5](CF_3SO_3)_3$ (**II**), in which ruthenium replaces iron. The much greater resolution in the spectrum of **II** is obvious. The simulation parameters give the deuterium content of **I** and **II** respectively as 18.8% and 18.4%, fwhm line widths as 4.23 and 1.58 Hz, equatorial ammine deuteration shifts as 20.20 and 17.51 ppb, and axial shifts as −36.24 and −31.55 ppb (SI, section S4). The corresponding T_1 relaxation times at 500 MHz are 125 and 171 ms. As expected, the resolution is enhanced in the spectrum of **I** at 950 MHz, compared with that at 500 MHz in Figure 3. However, there is also a difference in the line widths of **I**, which are 6.2 and 4.2 Hz at 500 and 950 MHz, respectively. This is consistent with the predictions of the Solomon equations for nuclei whose relaxation is due to dipolar coupling to unpaired electrons.[53]

The main differences between **I** and **II**, clearly visible in Figure 7, are a 13.3% reduction in both the axial and equatorial deuteration shifts and a much larger (65%) reduction in the line width in **II**. The reductions in the deuteration shifts correspond well to the estimated 14.8% decrease in the geometric factor for dipolar coupling in **II** (SI, section S5). It is clear from the energy of the charge-transfer transition in **II** that the extent of charge and therefore spin transfer is much reduced (SI, Table S5), and we therefore attribute the reduced line width to a reduction in the spin density on the donor metal in close proximity to the Cp protons. The importance of this

observation is that the prolific isotopomeric structure will not be resolvable in analogous compounds, in which the extent of charge transfer is relatively large. The complex $[(\eta^5\text{-}C_5H_5)Fe\text{-}(dppe)(\mu\text{-CN})Ru(NH_3)_5](CF_3SO_3)_3$ (SI, section S5), which has a much larger degree of charge transfer because of the replacement of carbonyls with the bidentate phosphine, exhibits a ^1H NMR spectrum with much larger line widths and unresolvable isotopic structure. Clearly, the detailed structure analyzed here is confined to compounds with very limited spin transfer across the bridge.

5. CONCLUSIONS

The isotopomeric detail reported in this work stems from some special electronic features.

(a) The Cp ^1H NMR line widths of **I**, at room temperature in water and acetone-d_6, are typically 5 ppb at 500 MHz, so that the 20 ppb shifts induced by a single ammine deuteration, and the smaller shifts due to vicinal effects, can be determined with good precision. This is a consequence of the short spin−lattice relaxation time of the low-spin Ru^{III} d^5 ion ($\sim10^{-11}$s)[54−56] relative to the period of the Larmor frequency ($>10^{-9}$ s).[53] The small extent of spin transfer across the bridge to the iron atom, whose close proximity to the Cp protons is an efficient source for their relaxation, is also significant. These characteristics will limit the generality with which the isotopomeric structure can be observed in this class of compounds.

(b) Several lines of evidence indicate that the isotopomeric HSs are dominated by dipolar coupling between the Cp proton nuclear moments and the anisotropy in the local electronic moment centered on the Ru^{III} ion.

(c) The sign and magnitude of the deuteration-induced shifts are different in axial and equatorial ammines. These are readily explained by changes in the **g**-value anisotropy linked to changes in the tetragonal component of the ligand field at the Ru^{III} ion.

(d) Surprisingly, large shifts (20−40 ppb) are caused by very small changes ($\sim2−3$ cm^{-1}) in the tetragonal field. The signs of these shifts indicate that deuterium substitution in an ammine ligand, making it a weaker π donor with respect to the Ru $t_{2g}(\pi)$ shell. Deuteration and an N−H anharmonic potential should result in a shorter and stronger bond and a concomitant weakening of the N−Ru π interaction. A computational study of the effect of deuteration will be required to understand these π-donor properties in detail, together with the origin of the vicinal effects.

(e) The remarkable sensitivity of the magnetic moment to changes in the tetragonal field can be attributed to the fact that the ground-state E' wave functions in an octahedral field contain a large orbital component. This is linked, in the second order, by the tetragonal field perturbation to the U' excited state whose proximity (~1425 cm^{-1}) ensures that consequential changes in the magnetic moment are substantial. This separation is determined by the spin−orbit coupling constant, which for the Ru^{3+} ion is large enough for the U' excited states to remain unpopulated but small enough to ensure that second-order perturbations are important.

(f) The proximity of the U' excited state is also responsible for the unusually large temperature-independent contributions to the HS.

Finally, we note that the proton resonances of the methyl groups in, for example, $[^tBu\text{-}C\equiv NRu(NH_3)_5]^{3+}$ ought to exhibit a similar sensitivity to the tetragonal field at the ruthenium center, while largely avoiding the line broadening
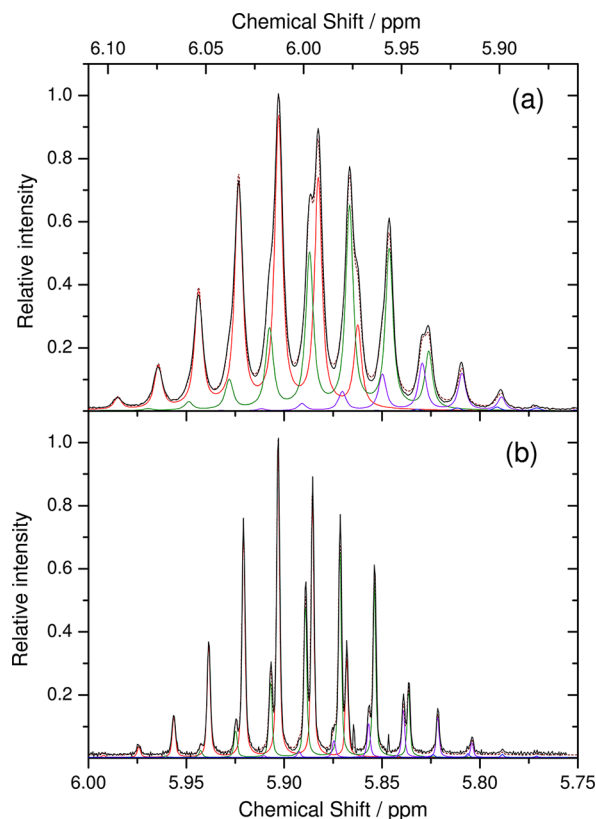
associated with the spin transfer described here. As such, they should act as a sensitive probe for the presence of any species that binds to the ammine ligands in acidic or nonaqueous solution or indeed for the presence of deuterons that can exchange with the ammine protons.

■ ASSOCIATED CONTENT

⑤ Supporting Information

Crystallographic data (CIF) file, selected bond metric data, EPR data, derivation of expressions for the contact and pseudocontact HSs, assigned spectrum of the minor impurity, computational geometry optimizations, orbital energies, and spin densities. This material is available free of charge via the Internet at http://pubs.acs.org.

■ AUTHOR INFORMATION

Corresponding Author

*E-mail: michael.laidlaw@chem.ox.ac.uk (W.M.L.), jennifer. green@chem.ox.ac.uk (J.C.G.).

Notes

The authors declare no competing financial interest.
∞(R.G.D.) Deceased on May 16, 2013.

■ ACKNOWLEDGMENTS

■ REFERENCES

(1) Laidlaw, W. M.; Denning, R. G. *Chem. Commun.* **2008**, 1590−1592.

(2) Laidlaw, W. M.; Denning, R. G.; Murphy, D. M.; Green, J. C. *Dalton Trans.* **2008**, 6257−6264.

(3) Robin, M. B.; Day, P. *Adv. Inorg. Radiochem.* **1967**, *10*, 247.

(4) Heintz, R. A.; Neiss, T. G.; Theopold, K. H. *Angew. Chem., Int. Ed. Engl.* **1994**, *33*, 2326−2328.

(5) Medforth, C. J.; Shiau, F. Y.; Lamar, G. N.; Smith, K. M. *J. Chem. Soc., Chem. Commun.* **1991**, 590−592.

(6) Wojaczynski, J.; Latos-Grazynski, L.; Hrycyk, W.; Pacholska, E.; Rachlewicz, K.; Szterenberg, L. *Inorg. Chem.* **1996**, *35*, 6861−6872.

(7) Nataro, C.; Chen, J. B.; Angelici, R. J. *Inorg. Chem.* **1998**, *37*, 1868−1875.

(8) Lawrence, G. A.; Lay, P. A.; Sargeson, A. M.; Taube, H. *Inorg. Synth.* **1986**, *24*, 257.

(9) Dixon, N. E.; Sargeson, A. M. *Inorg. Synth.* **1986**, *24*, 253.

(10) Cosier, J.; Glazer, A. M. *J. Appl. Crystallogr.* **1986**, *19*, 105−107.

(11) Otwinowski, Z.; Minor, W. Processing of X-ray Diffraction Data Collected in Oscillation Mode. In *Methods in Enzymology*; Carter, C. W., Sweet, R. M., Eds.; Academic Press: New York, 1997; p 276.

(12) Altomare, A.; Cascarano, G.; Giacovazzo, C.; Guagliardi, A.; Burla, M. C.; Polidori, G.; Camalli, M. *J. Appl. Crystallogr.* **1994**, *27*, 435.

(13) Betteridge, P. W.; Carruthers, J. R.; Cooper, R. I.; Prout, K.; Watkin, D. J. *J. Appl. Crystallogr.* **2003**, *36*, 1487.

(14) Cooper, R. I.; Thompson, A. L.; Watkin, D. J. *J. Appl. Crystallogr.* **2010**, *43*, 1100−1107.

(15) Spek, A. *J. Appl. Crystallogr.* **2003**, *36*, 7−13.

(16) Spek, A. L. *PLATON, A Multipurpose Crystallographic Tool*; Utrecht University: Utrecht, The Netherlands, 1998.

(17) Hwang, T. L.; Shaka, A. J. *J. Magn. Reson., Ser. A* **1995**, *112*, 275−279.

(18) Andrae, D.; Haeussermann, U.; Dolg, M.; Stoll, H.; Preuss, H. *Theor. Chem. Acc.* **1990**, *77*, 123−41.

(19) Frisch, M. J.; Trucks, G. W.; Schlegel, H. B.; Scuseria, G. E.; Robb, M. A.; Cheeseman, J. R.; Montgomery, J. A., Jr.; Vreven, T.; Kudin, K. N.; Burant, J. C.; Millam, J. M.; Iyengar, S. S.; Tomasi, J.; Barone, V.; Mennucci, B.; Cossi, M.; Scalmani, G.; Rega, N.; Petersson, G. A.; Nakatsuji, H.; Hada, M.; Ehara, M.; Toyota, K.; Fukuda, R.; Hasegawa, J.; Ishida, M.; Nakajima, T.; Honda, Y.; Kitao, O.; Nakai, H.; Klene, M.; Li, X.; Knox, J. E.; Hratchian, H. P.; Cross, J. B.; Bakken, V.; Adamo, C.; Jaramillo, J.; Gomperts, R.; Stratmann, R. E.; Yazyev, O.; Austin, A. J.; Cammi, R.; Pomelli, C.; Ochterski, J. W.; Ayala, P. Y.; Morokuma, K.; Voth, G. A.; Salvador, P.; Dannenberg, J. J.; Zakrzewski, V. G.; Dapprich, S.; Daniels, A. D.; Strain, M. C.; Farkas, O.; Malick, D. K.; Rabuck, A. D.; Raghavachari, K.; Foresman, J. B.; Ortiz, J. V.; Cui, Q.; Baboul, A. G.; Clifford, S.; Cioslowski, J.; Stefanov, B. B.; Liu, G.; Liashenko, A.; Piskorz, P.; Komaromi, I.; Martin, R. L.; Fox, D. J.; Keith, T.; Al-Laham, M. A.; Peng, C. Y.; Nanayakkara, A.; Challacombe, M.; Gill, P. M. W.; Johnson, B.; Chen, W.; Wong, M. W.; Gonzalez, C.; Pople, J. A. *Gaussian 03*, revision D.02; Gaussian, Inc.: Wallingford, CT, 2004.

(20) *ADF2010.02*; Theoretical Chemistry, Vrije Universiteit: Amsterdam, The Netherlands, 2009; http://www.scm.com

(21) te Velde, G.; Bickelhaupt, F. M.; Baerends, E. J.; Fonseca Guerra, C.; Van Gisbergen, S. J. A.; Snijders, J. G.; Ziegler, T. *J. Comput. Chem.* **2001**, *22*, 931.

(22) Fonseca Guerra, C.; Snijders, J. G.; te Velde, G.; Baerends, E. J. *Theor. Chem. Acc.* **1998**, *99*, 391.

(23) van Lenthe, E.; Baerends, E. J.; Snijders, J. G. *J. Chem. Phys.* **1993**, *99*, 4597.

(24) van Lenthe, E.; Baerends, E. J.; Snijders, J. G. *J. Chem. Phys.* **1994**, *101*, 9783.

(25) van Lenthe, E.; Snijders, J. G.; Baerends, E. J. *J. Chem. Phys.* **1996**, *105*, 6505.

(26) van Lenthe, E.; van Leeuwen, R.; Baerends, E. J.; Snijders, J. G. *Int. J. Quantum Chem.* **1996**, *57*, 281.

(27) van Lenthe, E.; van der Avoird, A.; Wormer, P. E. S. *J. Chem. Phys.* **1997**, *107*, 2488.

(28) van Lenthe, E.; van der Avoird, A.; Wormer, P. E. S. *J. Chem. Phys.* **1998**, *108*, 4783.

(29) Pye, C. C.; Ziegler, T. *Theor. Chem. Acc.* **1999**, *101*, 396.

(30) Klamt, A. *J. Phys. Chem.* **1995**, *99*, 2224.

(31) Klamt, A.; Jones, V. *J. Chem. Phys.* **1996**, *105*, 9972.

(32) Klamt, A.; Schüürmann, G. *J. Chem. Soc., Perkin Trans. 2* **1993**, 799.

(33) Meyer, T. J.; Taube, H. *Inorg. Chem.* **1968**, *7*, 2369−2379.

(34) Waysbort, D.; Navon, G. *J. Phys. Chem.* **1973**, *77*, 960−964.

(35) Brown, A.; Edmonds, J. W. *Adv. X-ray Anal.* **1980**, *23*, 361−374.

(36) Kurland, R. J.; McGarvey, B. R. *J. Magn. Reson.* **1970**, *2*, 286−301.

(37) Reynolds, P. A.; Delfs, C. D.; Figgis, B. N.; Engelhardt, L. M.; Moubaraki, B.; Murray, K. S. *J. Chem. Soc., Dalton Trans.* **1992**, 2029−2032.

(38) Laidlaw, W. M.; Thompson, A. L.; Denning, R. G. *Dalton Trans.* **2013**, *42*, 4695−4703.

(39) Laidlaw, W. M.; Denning, R. G. *Polyhedron* **1994**, *13*, 1875−1880.

(40) Gutmann, V. *Electrochim. Acta* **1976**, *21*, 661−670.

(41) Hush, N. S. *Prog. Inorg. Chem.* **1967**, *8*, 391.

(42) Dreuw, A.; Head-Gordon, M. *J. Am. Chem. Soc.* **2004**, *126*, 4007−4016.

(43) Kondov, I.; Vallet, V.; Wang, H. B.; Thoss, M. *J. Phys. Chem. A* **2008**, *112*, 5467−5477.

(44) Bertini, I.; Luchinat, C. *Coord. Chem. Rev.* **1996**, *150*, 29−75.

(45) Komi, Y.; Urushiyama, A. *Bull. Chem. Soc. Jpn.* **1980**, *53*, 980−982.

(46) Bendall, M. R.; Doddrell, D. M. *Aust. J. Chem.* **1978**, *31*, 1141−1143.

(47) Freeman, R.; Murray, G. R.; Richards, R. E. *Proc. R. Soc. London, Ser. A: Math. Phys. Sci.* **1957**, *242*, 455−466.

(48) Wesener, J. R.; Gunther, H. *Tetrahedron Lett.* **1982**, *23*, 2845−2848.

(49) Forsyth, D. A.; Botkin, J. H.; Osterman, V. M. *J. Am. Chem. Soc.* **1984**, *106*, 7663−7666.

(50) Forsyth, D. A.; Macconnell, M. M. *J. Am. Chem. Soc.* **1983**, *105*, 5920−5921.

(51) Forsyth, D. A.; Yang, J. R. *J. Am. Chem. Soc.* **1986**, *108*, 2157−2161.

(52) Griffith, J. S. *The Theory of Transition-Metal Ions*; Cambridge University Press: London, 1961.

(53) Bertini, I.; Luchinat, C. *Coord. Chem. Rev.* **1996**, *150*, 77−110.

(54) Serebrennikov, Y. A.; Steiner, U. E. *J. Chem. Phys.* **1994**, *100*, 7508−7514.

(55) Steiner, U. E.; Serebrennikov, Y. A. *J. Chem. Phys.* **1994**, *100*, 7503−7507.

(56) Burssner, D.; Wolff, H. J.; Steiner, U. E. *Z. Phys. Chem.: Int. J. Res. Phys. Chem. Chem. Phys.* **1993**, *182*, 297−308.